○ **Geothermal Energy**

RESEARCH

Thermally driven fracture aperture variation in naturally fractured granites

Marina Grimm Lima[1], Daniel Vogler[1], Lorenzo Querci[2], Claudio Madonna[3], Bodo Hattendorf[2], Martin O. Saar[1] and Xiang-Zhao Kong[1*] ○

*Correspondence:
xkong@ethz.ch
[1] Geothermal Energy
and Geofluids Group,
Institute of Geophysics, ETH
Zürich, Sonneggstrasse 5,
8092 Zurich, Switzerland
Full list of author information
is available at the end of the
article

Abstract

Temperature variations often trigger coupled thermal, hydrological, mechanical, and chemical (THMC) processes that can significantly alter the permeability/impedance of fracture-dominated deep geological reservoirs. It is thus necessary to quantitatively explore the associated phenomena during fracture opening and closure as a result of temperature change. In this work, we report near-field experimental results of the effect of temperature on the hydraulic properties of natural fractures under stressed conditions (effective normal stresses of 5–25 MPa). Two specimens of naturally fractured granodiorite cores from the Grimsel Test Site in Switzerland were subjected to flow-through experiments with a temperature variation of 25–140 °C to characterize the evolution of fracture aperture/permeability. The fracture surfaces of the studied specimens were morphologically characterized using photogrammetry scanning. Periodic measurements of the efflux of dissolved minerals yield the net removal mass, which is correlated to the inferred rates of fracture closure. Changes measured in hydraulic aperture are significant, exhibiting reductions of 20–75% over the heating/cooling cycles. Under higher confining stresses, the effects in fracture permeability are irreversible and notably time-dependent. Thermally driven fracture aperture variation was more pronounced in the specimen with the largest mean aperture width and spatial correlation length. Gradual fracture compaction is likely controlled by thermal dilation, mechanical grinding, and pressure dissolution due to increased thermal stresses exerted over the contacting asperities, as confirmed by the analyses of hydraulic properties and efflux mass.
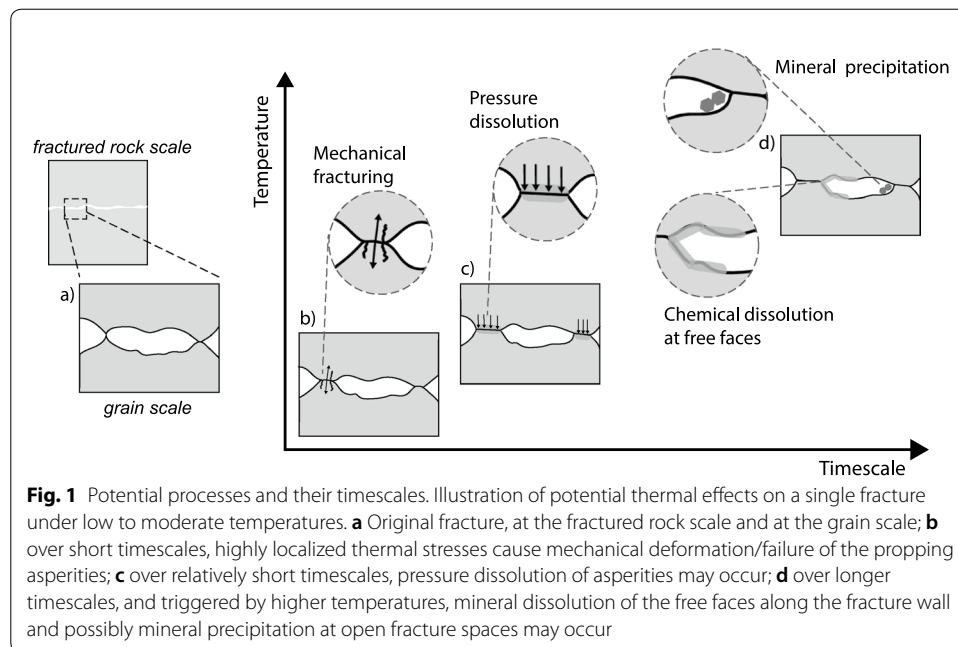
Keywords: Geothermal energy, Rough fracture, Fracture aperture evolution, Thermo-hydro-mechanical-chemical (THMC) effects, Pressure dissolution, Fracture flow, Fractured reservoirs

Introduction

Coupled thermal–hydrological–mechanical–chemical (THMC) processes can significantly impact the long-term evolution of reservoir permeability, associated with geothermal energy extraction (Bažant and Ohtsubo 1977; Pandey and Vishal 2017; Kamali-Asl et al. 2018), hydrocarbon production (Dobrynin 1962; Dusseault 2011; Liu et al. 2016), nuclear waste disposal (Tsang 1987; Nguyen et al. 1995), and geologic storage of carbon dioxide (CO_2) (Rutqvist and Tsang 2002; Kopp et al. 2009; Luhmann et al. 2012, 2014; Tutolo et al. 2014, 2015a, b; Zhang et al. 2015, 2016). In fractured

reservoirs, fractures often dominate the transport of mass and energy, as fracture permeabilities are typically orders of magnitude larger than those of the surrounding rock matrices. Particularly, the permeability of a fracture can easily and quickly change, however, as fractures may undergo opening or closure, due to changes in normal stress, pore-fluid pressure (Barton et al. 1985; Cook 1992; Huo and Benson 2016; Vogler et al. 2016, 2018; Kling et al. 2018), temperature (Morrow et al. 2001; Ghassemi and Kumar 2007), and/or chemical equilibrium (Polak et al. 2003; Yasuhara and Elsworth 2008). In general, the effect of an individual THMC process on fracture permeability changes cannot be fully decoupled from the others, as they all change the system state and trigger other system responses that can jointly lead to either opening or closure of a fracture. Fracture closure may significantly alter the reservoir hydraulic behavior, eventually leading to the failure of fracture-dominated geological reservoir operations (Stephansson et al. 1996; Elsworth and Yasuhara 2010). For example, enhanced geothermal systems (EGS) rely on sustaining a deep bedrock fracture network of sufficiently high permeability to provide continuous heat exchange between the fractured rock and the circulation fluid. In this scenario, coupled THMC effects might cause a decline in heat production and reduce or even prevent the feasibility of EGS operations under economically viable conditions. The hydraulic performance of fracture-dominated rocks is significantly more sensitive to THMC processes than that of intact rocks, and changes in the performance can span several orders of magnitude (Kranzz et al. 1979; Stephansson et al. 1996; Morrow et al. 2001). It is, therefore, necessary to investigate the coupling between mechanical, hydrological, thermal, and chemical processes in fractures to develop well-calibrated models and predict the changes in hydraulic and transport properties of deep, fracture-dominated geological reservoirs.

The effect of temperature on fracture permeability, under constant normal stress, has been recognized both in laboratory experiments (Morrow et al. 2001; Yasuhara et al. 2006; Luo et al. 2018) and during field tests (Hardin et al. 1982; Yow and Wilder 1993; Barton 2007; Rutqvist et al. 2008), even at moderate temperatures of 100–120 °C (Yasuhara et al. 2011; Faoro et al. 2016; Kamali-Asl et al. 2018). Fracture permeability has been reported to decrease monotonically with increasing temperature. For example, Polak et al. (2003) have observed reductions of ∼80% in hydraulic aperture widths in naturally fractured novaculite specimens, caused by thermal–chemical processes, during a 900-h flow-through experiment at 25–150 °C. Such temperature-driven fracture closure may result from reversible elastic compaction or irreversible mechanical fracturing of the propping asperities (Yasuhara et al. 2011; Faoro et al. 2016), chemical dissolution of the contacting asperities (Yasuhara et al. 2006; Faoro et al. 2016; Kamali-Asl et al. 2018), and/or clogging of the fracture void spaces by mineral precipitation (Morrow et al. 2001; Dobson et al. 2003; Caulk et al. 2016). While it is challenging to decouple the thermal–mechanical and chemically induced responses, it is generally accepted that chemical processes occur on an extended timescale, while mechanical processes may occur over a relatively short timescale (Yasuhara et al. 2011). Figure 1 shows schematically the potentially involved processes as a function of timescale, when a fractured rock undergoes a change in temperature (Fig. 1). These processes are discussed further in the next paragraphs.

Fig. 1 Potential processes and their timescales. Illustration of potential thermal effects on a single fracture under low to moderate temperatures. **a** Original fracture, at the fractured rock scale and at the grain scale; **b** over short timescales, highly localized thermal stresses cause mechanical deformation/failure of the propping asperities; **c** over relatively short timescales, pressure dissolution of asperities may occur; **d** over longer timescales, and triggered by higher temperatures, mineral dissolution of the free faces along the fracture wall and possibly mineral precipitation at open fracture spaces may occur

Thermal stresses may have different effects on permeability, depending on the confinement of the fractured rock. If the rock is mechanically constrained during the temperature increase, the rock tends to expand into the fracture voids, as the fractured rock is likely more compliant than the intact rock (Jaeger et al. 2007). This expansion might then cause a reduction of fracture permeability, due to the reduced fracture volume available to fluid flow. This thermally driven fracture closure is sometimes compared to fracture closure caused by an increase in normal stresses (Long et al. 1996). If the rock is free to expand (i.e., the rock is without constraint), an increase in temperature does not necessarily result in an increase in stresses, as the fracture void spaces actually tend to dilate, yielding an increase in fracture permeability. In deep geological reservoirs, however, rock fractures are not free to expand as they are commonly laterally constrained (Ruistuen et al. 1999), which causes fracture closure if temperature increases. Studies about thermal effects in laboratory flow-through experiments commonly enforce this mechanical constraint of the fractured rock sample by confining pressures (Caulk et al. 2016; Faoro et al. 2016; Kamali-Asl et al. 2018). Once temperature increases, this boundary condition results in fracture closure of the compliant fracture, and not expansion, which is in line with behavior expected to occur at subsurface reservoir conditions.

At moderate temperatures of 100–120 °C, the impact of thermal effects on the fracture void space is usually more pronounced than that on the intact rock mass. The Young's modulus of granite, which is a property of the bulk material, tends to decrease with temperature. However, the reduction of the Young's modulus in granites is only significant for high temperatures of ∼100 °C (Toeroek and Toeroek 2015; Yin et al. 2016). In contrast, in fractured rocks, increases in temperature of ∼100 °C can already create local stress concentrations that induce mechanical fracturing (Faoro et al. 2016). A better understanding regarding such localized stresses could be

Lima *et al. Geotherm Energy*   (2019) 7:23

Page 4 of 28

achieved by interpreting natural fractures as two rough surfaces that are in contact at asperities (Fig. 1). Increased temperature in a fractured specimen will cause thermal dilation into the void fracture space as well as thermal stresses, which in turn manifest at the contacting asperities as compressive stresses. These stressed asperities can then undergo elastic/plastic deformation or fracturing from tensile loading, which is modeled as mechanical creep. This mechanical effect can be enhanced by chemical reaction if water is present, in which case the process is termed stress corrosion (Yasuhara and Elsworth 2008). Nevertheless, failure of contacting asperities, due to mechanical effects, are observed at moderate temperatures as low as 90 °C (Yasuhara et al. 2011), while other thermal effects on intact rock usually require much higher temperatures to become significant.
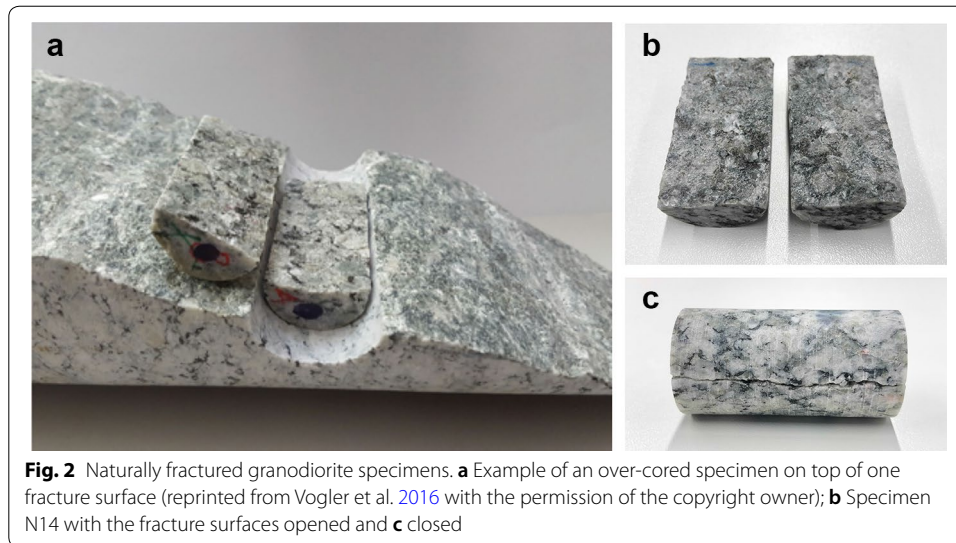
Higher stress concentrations at the contacting fracture asperities can also cause pressure dissolution (or pressure solution) creep processes (Polak et al. 2003; Yasuhara et al. 2004; Taron and Elsworth 2010; Lang et al. 2016). Pressure dissolution creep is a deformation mechanism involving chemical dissolution, caused by larger normal stress conditions, which predominantly occurs at the asperities of the rock fracture surfaces under increasing temperature conditions. This mechanism has been observed in laboratory flow-through experiments with several fractured rock types, including granite (Moore et al. 1994; Yasuhara et al. 2011; Kamali-Asl et al. 2018). Yasuhara et al. (2011) conducted a series of flow-through experiments with artificially fractured granite specimens under a constant mechanical stress state but with increasing temperatures (up to 90 °C) for 888 h (Yasuhara et al. 2011). The decrease in permeability observed at 90 °C was associated with mass removal due to mineral dissolution at the bridging asperities within the fracture, or pressure dissolution. Mechanical fracturing is considered to occur faster than pressure dissolution creep (Yasuhara and Elsworth 2008), but both mechanisms can be observed on short timescales (Fig. 1). Nevertheless, pressure dissolution is certainly a time-dependent process, and its kinetics must be considered in studies of the thermal effects on fracture permeability and during THMC modeling (Elliott and Rutter 1976).

For longer timescales, increasing temperature might also enhance chemical dissolution of the free faces along the fracture wall and may cause further mineral precipitation (Fig. 1). These mineral dissolution/precipitation reactions can lead to an increase or decrease of fracture permeability, depending on where precisely in the aperture field the reactions occur (Savage et al. 1992; Yasuhara et al. 2005; Yasuhara and Elsworth 2008; Elsworth and Yasuhara 2010; Ameli et al. 2014; Kim et al. 2015). Free-face dissolution is expected to increase the permeability of the fractured rock, as larger mechanical apertures are generated. In contrast, the precipitation of minerals in critical regions (e.g., "bottle necks") causes fracture closure or local blockage, resulting in a decrease in permeability. Mineral precipitation induced by increasing temperature has been identified in laboratory experiments (Morrow et al. 2001; Dobson et al. 2003; Caulk et al. 2016) and numerical simulations (Lowell et al. 1993; Martin and Lowell 2000; Kumar and Ghassemi 2005; Ghassemi and Kumar 2007) as the cause of hydraulic aperture decreases. Morrow et al. (2001) observed decreases of 80–90% in fracture transmissivity after 1000 h during a flow-through laboratory experiment at 150 °C, which were associated with mineral precipitation. The accumulated impact of mineral

dissolution or precipitation at free mineral surfaces on fracture permeability usually requires considerably more time to occur than mechanical or pressure dissolution creep, for example, due to typically slow reaction kinetics. Laboratory flow-through experiments investigating chemical processes are, therefore, usually conducted over long durations, such as 400 to 1000 h (Morrow et al. 2001; Polak et al. 2003; Yasuhara et al. 2004, 2011). In these experiments, the fracture permeability can deviate from a monotonic decrease with increasing temperature, if mineral dissolution at free mineral surfaces becomes the dominant process.

Thermally driven effects on fracture permeability seem to exhibit hysteretic behavior, which has been observed in laboratory (Kranzz et al. 1979; Faoro et al. 2016; Kamali-Asl et al. 2018) as well as field and block tests (Barton 1982). Barton (2007) has termed this response thermal *overclosure*, arguing that thermal effects accentuate stress-related fracture closure hysteresis. Heating a rock fracture promotes thermal dilation of the different minerals, usually resulting in a better fit of the fracture surfaces and an increase of friction at the contacting asperities (Barton 2007). When the rock is cooled back down, frictional and mating effects on fracture surfaces may cause irreversible permeability changes, even at low temperatures. In addition to mechanical effects, pressure dissolution may also contribute to the irreversibility of thermally driven fracture closures, as it results in an increase in the contact area of the fracture surfaces and ultimately a decrease in stress concentrations at the contacting asperities, thereby permanently disturbing the state of stress (Yasuhara and Elsworth 2008). Flow-through experiments by Faoro et al. (2016) on fractured granite specimens showed thermally induced hysteretic effects, with an irreversible change of the hydraulic aperture from 43 to 16 μm, after subjecting the specimens to 150 °C and subsequently cooling them down to the initial temperature of 25 °C. It is thus expected that the pronounced mechanical component during thermal hysteresis may even cause hysteretic effects on short timescales.

Additionally, the response of a rock fracture to THMC processes also depends on the morphology of the fracture surfaces (Pyrak-Nolte and Morris 2000). Size and spatial distribution of mechanical apertures as well as contact areas directly influence the hydraulic characteristics of the fracture, where large mean mechanical apertures and pronounced roughnesses tend to result in higher hydraulic conductivities and larger hydraulic aperture variations when mechanical loads change (Bandis et al. 1983; Luo et al. 2017). The spatial correlation of fracture aperture fields is also expected to play a significant role in the response of the fracture to increased compressive stresses, as a high spatial correlation results in preferential flow channels. Moreover, well-correlated fractures exhibit limited contact area, tend to be more compliant, and, therefore, open or close more readily (Pyrak-Nolte and Morris 2000). Pressure dissolution, on the other hand, is anticipated to be more pronounced when contact areas are smaller, as smaller areas result in higher stress concentrations. Yasuhara and Elsworth (2008) suggest that stress-driven fracture closure is influenced by the contact-area ratio of the aperture distribution, corresponding to the stress intensity factor. Therefore, the characterization of the fracture morphology, when available, aids in the prediction of how the rock will respond to changes in normal stresses or temperature and how the fluid will flow through the changing rock fracture.

Fig. 2 Naturally fractured granodiorite specimens. **a** Example of an over-cored specimen on top of one fracture surface (reprinted from Vogler et al. 2016 with the permission of the copyright owner); **b** Specimen N14 with the fracture surfaces opened and **c** closed
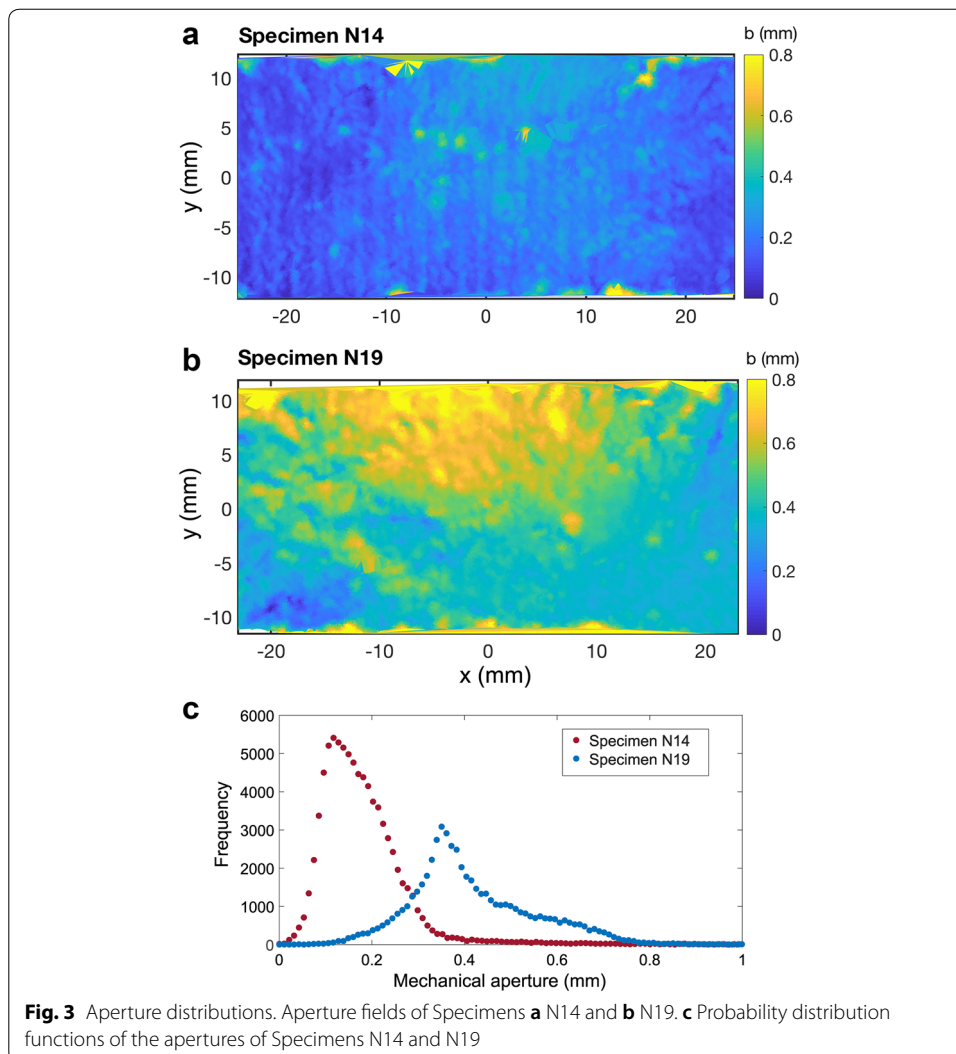
Despite the inspiring results reported by the aforementioned studies, thermal effects on fracture permeability still remain difficult to predict, mainly due to the complexity of coupled THMC processes and the differences in fractures. In particular, laboratory investigations on thermal effects on naturally fractured granite specimens are rarely reported. Relevant studies have been performed with specimens which were artificially fractured in the laboratory, and these specimens typically exhibit fracture surface topographies that are different from naturally fractured rocks. The "freshly made" fractured specimens may present different chemical reactivity when compared to natural fractures that have been "open" for longer periods of time, which might influence the response of the fracture to temperature changes (Blaisonneau et al. 2016; Gale 1982). Hence, the main purpose of this study is to investigate the impact of thermal effects on the hydraulic properties of natural granodiorite fractures during temperature variations of 25–140 °C and during near-field stress conditions. We present results from our reactive flow-through experiments, conducted on cylindrical granodiorite cores from the deep underground geothermal (DUG) Lab at the Grimsel Test Site (GTS), Switzerland (Amann et al. 2018). The specimens are split by a single natural tensile fracture parallel to the core axis (i.e., the mean flow direction). Photogrammetry scans of the specimen fracture surfaces provide morphological information. During the experiments, the evolution of the hydraulic aperture of the fracture is measured as a function of the imposed change of temperature. Furthermore, effluent chemical analyses are performed to assess the influence of chemical reactions on the variations in hydraulic responses. The obtained results assist the evaluation of THMC processes in fracture-dominated reservoirs under subsurface conditions.

Materials and methods

Granodiorite characterization

Our experiments used naturally fractured granodiorite cores from the Deep Underground Geothermal Lab at the Grimsel Test Site in Switzerland (Amann et al. 2018; Vogler et al. 2016, 2017a; Vogler 2016; Tanaka et al. 2014) (Fig. 2). Two tensile-fracture

Fig. 3 Aperture distributions. Aperture fields of Specimens **a** N14 and **b** N19. **c** Probability distribution functions of the apertures of Specimens N14 and N19

(Mode I) specimens (Vogler et al. 2016), namely N14 and N19, each with a diameter of 2.5 cm and a length of about 5.0 cm, were over-cored for the flow-through experiments (Fig. 2b, c). The rock composition by volume of the Grimsel granodiorite has been identified as follows: ~30% quartz, ~30% plagioclase, ~25% potassium feldspar, ~15% biotite, and minor amounts of white mica and chlorite (Stalder 1964; Schaltegger 1989).

Before the flow-through experiments commenced, the surfaces of the specimen fractures were characterized employing high-resolution photogrammetric scans with an ATOS Core 3D scanner (GOM GmbH) (Vogler et al. 2017a, b; GOM 2019). Similar to Vogler et al. (2018), the zero-stress fracture apertures were determined by performing surface alignments of the scanned surfaces. The aligned zero-stress mechanical aperture values are shown as their spatial distributions in Fig. 3, for both specimens. Table 1 lists the length and width of the aperture fields of the specimens and their aperture distribution parameters, and Fig. 3 shows the probability distribution functions of apertures of Specimens N14 and N19. In this study, the spatial aperture correlation lengths are calculated as the width at which the power spectral density (PSD) of the aperture spatial

Lima *et al. Geotherm Energy* (2019) 7:23

Page 8 of 28

Table 1 Specimen properties

Specimen	L (mm)	w (mm)	Fracture type	b_{mean} (mm)	σ (mm)	L_{c_x} (–)	L_{c_y} (–)
N14	49.7	25.0	Tensile	0.184	0.122	0.02	0.04
N19	46.0	24.5	Tensile	0.414	0.132	0.08	0.06

Physical properties of the specimens under investigation, where L and w are the length and width of the aperture field of the specimen, respectively, b_{mean} and σ are the mean and the standard deviation of the aperture distributions, respectively, L_{c_x} is the normalized correlation length in the flow direction, and L_{c_y} is the normalized correlation length in the direction perpendicular to the flow
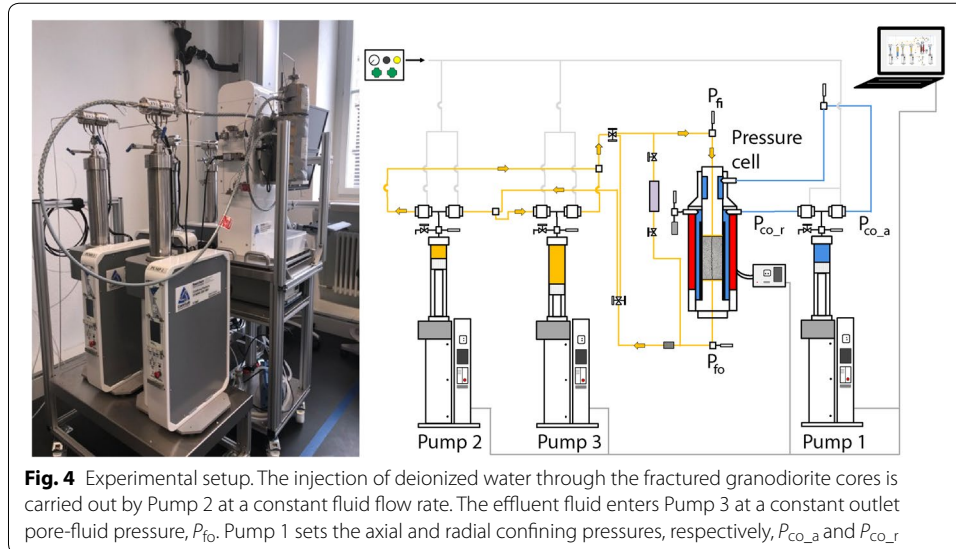
Fig. 4 Experimental setup. The injection of deionized water through the fractured granodiorite cores is carried out by Pump 2 at a constant fluid flow rate. The effluent fluid enters Pump 3 at a constant outlet pore-fluid pressure, P_{fo}. Pump 1 sets the axial and radial confining pressures, respectively, P_{co_a} and P_{co_r}

distribution (Fig. 3) reaches one half of the PSD peak value, or full width at half max (FWHM) (Brown et al. 1986; Domenico and Schwartz 1990; Jacobs et al. 2017; Pyrak-Nolte and Morris 2000). The calculated spatial correlation lengths were further normalized by the length and width of each specimen (Table 1).

Experimental setup

The experimental setup consisted of a standard triaxial pressure cell (designed for 2.5-cm cores of length up to 5.1 cm and pore pressures up to 35 MPa) (Fig. 4). Three high-performance volumetric pumps (Model Stigma 300D, pressure range of up to 100 MPa, 0.1% FS accuracy) were utilized to control the radial and axial confining pressures p_{co_r} and p_{co_a} (Pump 1), respectively, the fluid pressure at the specimen outlet, p_{fo} (Pump 3), and the injection volumetric flow rate, Q (Pump 2). In the cell, the ratio $p_{co\_a} = 1.13 \times p_{co\_r}$ is established when both confining pressures are supplied by the same pump, which was the case in this study. Since the rock sample is fixed between axial pistons (Fig. 5), the small nonzero deviatoric stress resulting from the difference between the axial and radial pressures is not expected to lead to shearing effects (Gentier et al. 2000; Lee et al. 2014). While establishing the injection flow rate, Pump 2 also measured the pressure at the specimen inlet, p_{fi}. Pressures and flow rate were recorded via a Falcon® control software. A pressure transducer, Keller PAA-33X (resolution of 0.05%

Fig. 5 Fractured specimen confinement. Specimen confined within **a** heat-shrinkable and **b** rubber sleeves, before being placed into the pressure cell

FS), provided additional measurements of the pressure differences between the specimen outlet and inlet. The pressure cell has a built-in heating system, which elevates the cell temperature to set points at specific rates. The injected fluid was therefore preheated to the cell temperature before reaching the specimen. Insulation around the cell inlet and the cell body assured that the injected fluid temperature is maintained at that of the specimen. A complete description of the flow-through system is provided in Ma et al. (2019).

A set of preliminary tests showed that our system can reach a maximum temperature of ∼140 °C, given the pressure that was applied in this study. Attempts to reach higher temperatures caused confining pressure loss due to rupturing of the confining sleeve. In order to allow the system to operate under these high temperature and pressure conditions, special confinement of the specimen in the cell was implemented. The two half rock specimens were carefully fitted together and confined first within a heat-shrinkable sleeve (Fig. 5a), and later additionally wrapped with a rubber AFLAS sleeve (Fig. 5b). In this study, the specimens were placed in the pressure cell with the fracture oriented parallel to the pressure cell axis (Fig. 5a), resulting in fluid flow along the fracture from the fluid inlet to the outlet. Similar set-ups to investigate rock specimen properties were employed by Yasuhara et al. (2011), Faoro et al. (2016), and Vogler et al. (2016).

Experimental procedure

A total of five flow-through experiments were conducted under a constant downstream pore-fluid pressure of 15 MPa (i.e., constant back pressure), radial confining pressures of 20, 30, and 40 MPa and temperatures of 25 °C to 140 °C. Before the experiments, deionized (milli-Q®) water was filled into Pump 2 as injection fluid.
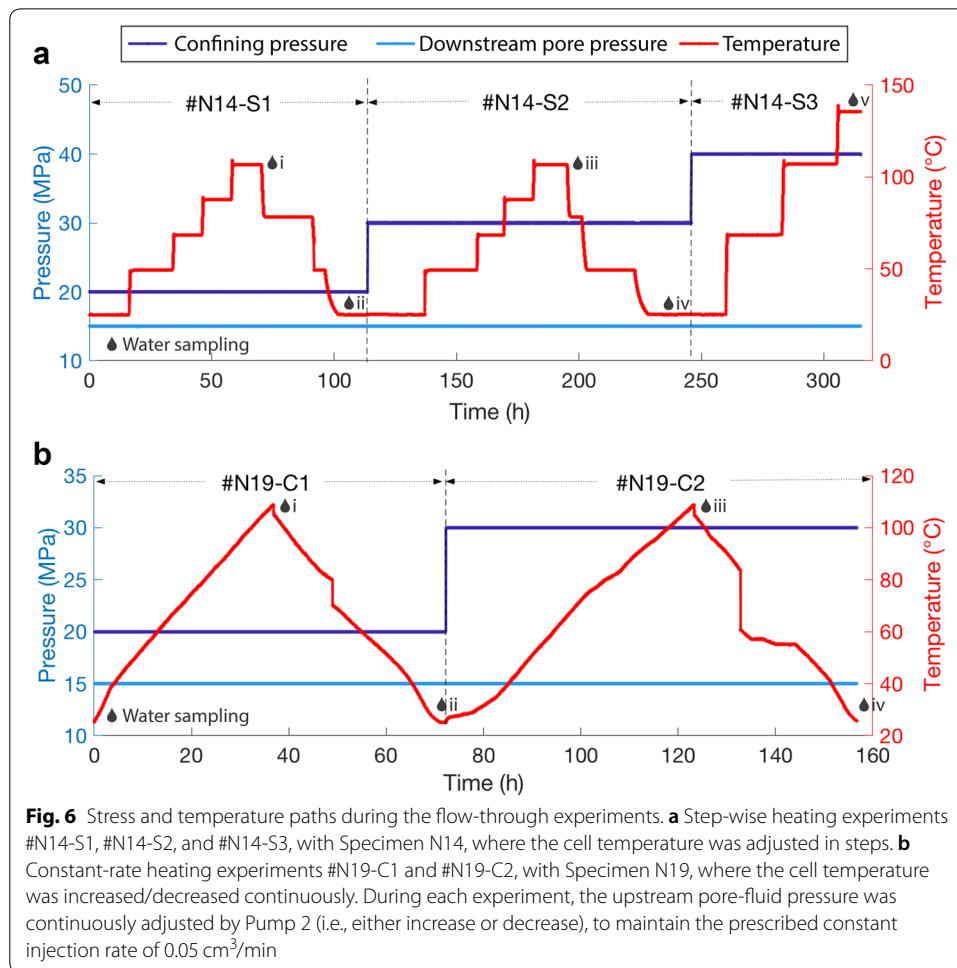
Table 2 Experiment specifications

Type of heating	Specimen	Test name	P_{co_r} (MPa)	Temperature (°C)	Duration (h)
Step-wise heating	N14	#N14-S1	20	[25, 50, 70, 90, 110, 80, 50, 25]	115
		#N14-S2	30	[25, 50, 70, 90, 110, 80, 50, 25]	137
		#N14-S3	40	[25, 70, 110, 140]	83
Constant-rate heating	N19	#N19-C1	20	[25 → 110 → 25]	92
		#N19-C2	30	[25 → 110 → 25]	101

All experiments were conducted under a constant back pressure of 15 MPa and a constant flow rate of 0.05 cm^3/min. P_{co_r} stands for radial confining pressure

During the experiments, the injection flow rate was kept constant at 0.05 cm^3/min by Pump 2 (0.1% FS volume accuracy), which operated in a displacement-control mode, while Pumps 1 and 3 operated in a stress-control mode, establishing constant confining pressure and back pressure, respectively. The relevant experimental conditions are listed in Table 2. We conducted two main groups of experiments: experiments #N14-S1, #N14-S2, and #N14-S3, where the cell temperature was changed step-wise, and experiments #N19-C1 and #N19-C2, where the heater was programmed to change the cell temperature at a constant rate. These two different set-ups were designed to allow us to evaluate the impact of time-dependent effects on fracture permeability, along with temperature-dependent effects, as the two types of experiments differ in the amount of time the specimen is exposed to the new temperature condition.

During experiments #N14-S1 and #N14-S2, the cell temperature was stepped up to 110 °C and then back down to 25 °C as follows: 25–50, 50–70, 70–90, 90–110, 110–80, 80–50, and 50–25 °C. During experiment #N14-S3, the cell temperature was stepped up to 140 °C as follows: 25–70, 70–110, 110–140 °C. In all experiments, each temperature step lasted an average of 19 h. These three experiments, namely #N14-S1, #N14-S2, and #N14-S3, were conducted with Specimen N14 and in sequence, without taking the specimen out of the pressure cell. The main difference between these three experiments was the radial confining pressure. The radial confining pressure started at 20 MPa in experiment #N14-S1, was then increased to 30 MPa during experiment #N14-S2, and was further increased to 40 MPa during experiment #N14-S3. Each change of confining pressure was followed by an average of 24 h of flow at constant temperature of 25 °C and constant injection rate of 0.05 cm^3/min, to allow the fracture surfaces to equilibrate with the new stress field state before the temperature was changed. Figure 6a summarizes the stress and temperature paths of these three experiments.

Experiments #N19-C1 and #N19-C2 were conducted with Specimen N19. However, unlike the first group of experiments, the cell temperature was changed continuously in these tests, controlled by the built-in heating system. The continuous temperature change was applied from 25 to 110 °C and then back to 25 °C. On average, the temperature variation was 1.8 °C/h. In analogy to the first group of experiments, these two experiments were conducted in sequence, without taking Specimen N19 out of the pressure cell. The radial confining pressure started lower, at 20 MPa, in experiment #N19-C1 and was then increased to 30 MPa during experiment #N19-C2. The change of confining stress was made at 25 °C, while the flow rate was kept constant at

Fig. 6 Stress and temperature paths during the flow-through experiments. **a** Step-wise heating experiments #N14-S1, #N14-S2, and #N14-S3, with Specimen N14, where the cell temperature was adjusted in steps. **b** Constant-rate heating experiments #N19-C1 and #N19-C2, with Specimen N19, where the cell temperature was increased/decreased continuously. During each experiment, the upstream pore-fluid pressure was continuously adjusted by Pump 2 (i.e., either increase or decrease), to maintain the prescribed constant injection rate of 0.05 cm^3/min

this temperature for 16 h to reach steady-state conditions under the higher compressive-stress condition before the change in temperatures. Figure 6b summarizes the stress and temperature paths of these two experiments.

During the flow-through experiments, the differential pressure, measured across the specimens, provided a continuous record of the fracture permeability at various temperatures. It is reasonable to assume that the granodiorite matrix has negligible porosity (Kamali-Asl et al. 2018) and a virtually impermeable matrix. Therefore, fluid flow occurred almost exclusively through the single, rough fracture within the specimens. Under the assumption of the cubic law (Oron and Berkowitz 1998; Witherspoon et al. 1980), the temperature-dependent volumetric flow rate, Q (m^3 s^{-1}), is proportional to the hydraulic pressure gradient, $\Delta p/L$ (Pa m^{-1}), with a coefficient of the product of fracture properties, including fracture width, w [m], and temperature-dependent hydraulic aperture, b_{hyd} (m),

$$Q_{(T)} = -\frac{w b_{\text{hyd}(T)}^3 \Delta p}{12 \mu_{(T)} L},$$

(1)

where μ (Pa s) is the temperature-dependent dynamic fluid viscosity. The fracture permeabilities , k_f (m²), can be obtained from the hydraulic aperture values, as $k_f = b_{hyd}^2/12$. It is worth to note that the hydraulic aperture of a rough-walled fracture (b_{hyd}) is invariably lower than its mean mechanical aperture (b_{mean}) (Jaeger et al. 2007; Zimmerman et al. 1991; Renshaw 1995). This difference is large if the variable-aperture fracture exhibits significant roughness and heterogeneity, as these aspects usually decrease the fracture permeability, and in which case b_{mean} is less representative of a fracture with uniform opening as assumed by the parallel plate model (b_{hyd}). The temperature-dependent dynamic water viscosity and water density values (i.e., fluid flow rate) were corrected using the temperature in the triaxial cell to allow the hydraulic aperture to be correctly estimated from the differential pressure measured.

Studies have shown that this linear relationship between Q and Δp (Eq. 1) is plausible when the flow within the fracture is laminar and the Reynolds number (Re) for flow in a single fracture (Eq. 2) is less than 1 (Brush and Thomson 2003),

$$Re = \frac{\rho \cdot l_v \cdot U_i}{\mu} = \frac{\rho \cdot b_{mean} \cdot Q}{\mu \cdot b_{mean} \cdot w} = \frac{\rho \cdot Q}{\mu \cdot w}, \tag{2}$$

where ρ (kg m^{-3}) is the density of the fluid, l_v (m) is the characteristic length of the viscous forces, μ (Pa s) is the dynamic fluid viscosity, U_i (m s^{-1}) is the characteristic velocity for inertial forces, and b_{mean} (m) is the mean aperture width. In this study, the Reynolds number was consistently smaller than 0.17 throughout the experiment duration, permitting the use of the cubic law to evaluate the fractures' hydraulic apertures.

Additionally, at the end of each cycle of increasing/decreasing temperature, the receiving pump was emptied and fluid samples were collected for chemical analyses. This procedure allowed the analysis of the ion concentrations to be associated with a single, finished cycle. Cation concentrations were determined by means of inductively coupled plasma-optical emission spectrometry (ICP-OES), and more details about the measurements can be found in Additional file 1. The results were assigned to the average ion concentration of each increasing/decreasing temperature cycle, C_p (kg m^{-3}), as given by

$$C_p(t_s) = \frac{\int_{0*}^{t_s} Q(t) \cdot C_p(t) dt}{\int_{0*}^{t_s} Q(t) dt}, \tag{3}$$

where 0* is the time when a new cycle of increasing/decreasing temperature has started and t_s is the cycle duration. Influent concentrations were subtracted from effluent concentrations to determine the concentration increases.

The effluent dissolved mass during each cycle is calculated by multiplying the measured ion concentrations and the total volume of the effluent fluid. This dissolved mass is ultimately used to estimate the total volume of dissolved minerals and to associate this dissolved mineral volume with a decrease in hydraulic aperture width, as explained in the next paragraphs. This association is performed by employing a model for which some assumptions are required. The first assumption is that the specimens are composed by six main, well-mixed minerals, present in certain percentages, as listed in Table 3. The second assumption is that all well-mixed minerals dissolve simultaneously, according to their

Table 3 Granodiorite mineral composition

Phase	Mineral	Formula	f_n[a]	$\chi_{Si,n}$[b]	ρ_n[b] ($kg\,m^{-3}$)
Quartz	Quartz	SiO_2	0.300	0.467	2648
Plagioclase	Albite	$NaAlSi_3O_8$	0.150	0.201	2620
	Anorthite	$CaAl_2Si_2O_8$	0.150	0.321	2730
K-feldspar	Microcline feldspar	$KAlSi_3O_8$	0.125	0.302	2620
	Orthoclase	$KAlSi_3O_8$	0.125	0.302	2560
Biotite	Annite	$KFe_3AlSi_3O_{10}(OH)_2$	0.150	0.164	3260

Mineral composition considered for the calculation of fracture aperture changes, due to chemical mineral dissolution, where f_n is the mineral volume fraction of the n-th mineral, $\chi_{Si,n}$ is the mass fraction of Si per mol of mineral n, and ρ_n is the density of mineral n

[a] Grimsel granodiorite: ~30% quartz, ~30% plagioclase, ~25% K-feldspar, ~15% biotite, and minor amounts of white mica and chlorite (Stalder 1964; Schaltegger 1989)

[b] Source: SciFinder: Database of chemicals (2019)

volume percentages. The third assumption is that the chemical formulas of the minerals are as discussed next. The plagioclase phase is assumed to be a solid solution of two end-members, namely albite and anorthite, with unknown volume percentages. Because the mineral densities and Si mole fractions of albite and anorthite are very similar (Table 3), we simply assume equal percentages of albite and anorthite in the plagioclase phase. Similarly, the K-feldspar phase is considered to be composed of equal amounts of microcline and orthoclase. Additionally, given that the black mica minerals, classified as biotite, have very similar physical properties, annite was chosen as a representative biotite to be used in our chemical calculations. The dissolution of these minerals will contribute to an increase in silicon ion concentration measured in the effluent samples. The fourth assumption is that a simplified fracture closure, derived from chemical dissolution, db_{chem}/dt ($m\,s^{-1}$), can be modeled by assuming that pressure dissolution was the dominant mineral dissolution process. Under these assumptions, the total volume of dissolved minerals, V_{diss} (m^3), can be computed by Caulk et al. (2016)

$$V_{diss} = \sum_{i=1}^{n} \left[\frac{f_n \cdot C_{Si} \cdot Q \cdot \Delta t}{\chi_{Si,n} \cdot \rho_n} \right], \tag{4}$$

where V_{diss} (m^3) is the total volume of dissolved minerals during a cycle of duration Δt, C_{Si} ($kg\,m^{-3}$) is the concentration of silicon in the effluent, calculated using Eq. 3, f_n ($m^3\,m^{-3}$) is the n-th mineral volume fraction of the GTS granodiorite specimen (Table 3), ρ_n ($kg\,m^{-3}$) is the density of mineral n, $\chi_{Si,n} = M_{Si} \times x_{Si}/M_n$ ($kg\,kg^{-1}$) is the mass fraction of Si per mol of mineral n, x_{Si} (–) is the number of atoms of Si in mineral n, and M_{Si} ($kg\,mol^{-1}$) and M_n ($kg\,mol^{-1}$) are the molar weights of Si and of mineral n, respectively. Hence, the fracture aperture change due to mineral dissolution, Δb_{chem} (m), can be calculated assuming that all the volume of dissolved minerals originates from fracture propping asperities, employing Caulk et al. (2016)

$$\Delta b_{chem} = \frac{V_{diss}}{A_c}, \tag{5}$$

where the contact area, $A_c = R_c A_f$ (m^2), is defined as the product of the entire fracture surface area, A_f (m^2), and the fractional contact area, R_c ($m^2\,m^{-2}$). Four different

estimated values of R_c are used in this study: 1, 5, 15, and 40% (Kamali-Asl et al. 2018; Faoro et al. 2016). Finally, the fracture closure rate , db_{chem}/dt (m s^{-1}), can be calculated by (Polak et al. 2003; Faoro et al. (2016; Caulk et al. 2016; Kamali-Asl et al. 2018)

$$\frac{db_{chem}}{dt} = -\sum_{n=1}^{6} \left[\frac{f_n}{\chi_{Si,n}} \cdot \frac{Q \cdot C_{Si}}{A_c \cdot \rho_n} \right]. \tag{6}$$
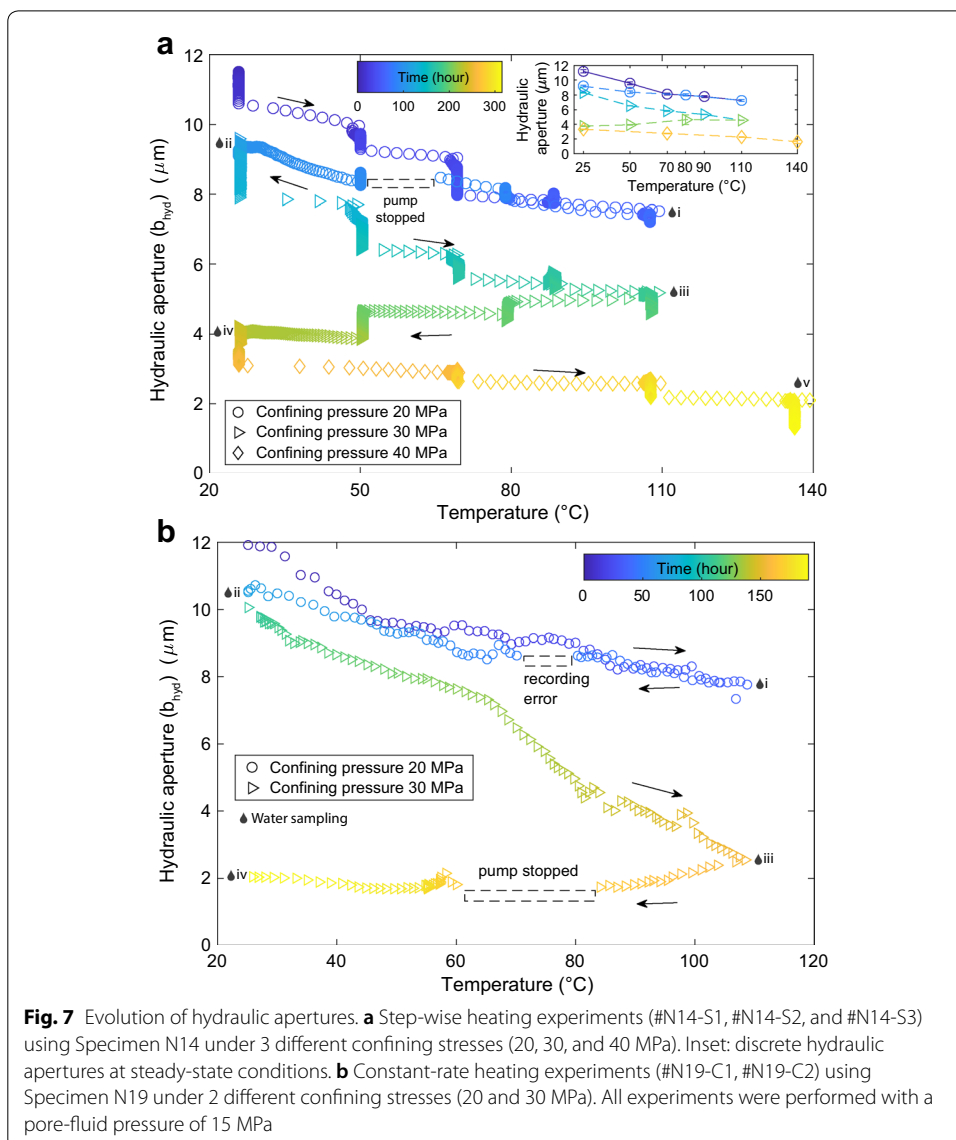
The minus sign on the right side of Eq. 6 means that, in our model, dissolution causes fracture *closure*, not opening. This notion was also previously adopted in other studies (Caulk et al. 2016) and relies on measurements that associate mineral dissolution with fracture sealing, not fracture opening (Yasuhara et al. 2011). Here, we consider a total of 6 minerals, as listed in Table 3.

Results and discussion

Hydraulic measurements and analyses

Figure 7a shows the hydraulic apertures, b_{hyd} (m), according to Eq. 1 of Specimen N14, inverted from the results of Experiments #N14-S1, #N14-S2, and #N14-S3, as a function of temperature. These three experiments were conducted in sequence, over a total duration of 335 h. The experimental progression in time is color coded in Fig. 7a. The vertically clustered discrete data points in Fig. 7a correspond to the temperature plateaus in Fig. 6. Each discrete temperature step lasted an average of 19 h in this group of experiments. Additionally, discrete hydraulic apertures, b_{hyd} (m), were estimated for each discrete temperature step, after the differential pressure, Δp (Pa), had reached a steady value. These discrete hydraulic apertures are shown in the inset, at the top right of Fig. 7a. Note that an interruption in data recording for almost 15 h occurred when the cell was cooling down under a confining pressure of 20 MPa. Figure 7b shows the hydraulic apertures of Specimen N19, derived from the results of Experiments #N19-C1 and #N19-C2 as a function of temperature. These two experiments were also conducted in sequence, over a total duration of 190 h. The experimental progression in time is also color coded in Fig. 7b. Note that during the two cooling cycles, there was a recording error for ~5 h under a confining pressure of 20 MPa and a pump stoppage for ~12 h under the 30 MPa of confining pressure. These two recording interruptions are also shown as vertical temperature curves in Fig. 6b. It is important to note that the pump stoppages did not induce pressure losses in the pressure cell. Aperture values for Specimens N14 and N19 were determined as 11 μm and 12 μm for the hydraulic apertures at 5 MPa effective normal stress at the beginning of the experiment and 195 μm and 424 μm for the mechanical aperture at zero stress, with deviations explained by the significant increase in effective normal stress and the reduction of flow rates by highly heterogeneous aperture fields.

During the experiments, fracture permeability decreases monotonically with an increase in temperature for all specimens and confining stress conditions (Fig. 7). Under 20 MPa of confining pressure, a temperature increase from 25 to 110 °C caused the hydraulic aperture to decrease from 11.2 to 7.3 μm for Specimen N14, and from 12.0 to 7.7 μm for Specimen N19. Under 30 MPa of confining pressure, the variation in temperature caused the hydraulic aperture of Specimen N14 to decrease from 8.3 to 4.6 μm

Fig. 7 Evolution of hydraulic apertures. **a** Step-wise heating experiments (#N14-S1, #N14-S2, and #N14-S3) using Specimen N14 under 3 different confining stresses (20, 30, and 40 MPa). Inset: discrete hydraulic apertures at steady-state conditions. **b** Constant-rate heating experiments (#N19-C1, #N19-C2) using Specimen N19 under 2 different confining stresses (20 and 30 MPa). All experiments were performed with a pore-fluid pressure of 15 MPa

during the heating cycle (i.e., from 25 to 110 °C), and then further to 3.7 µm at the end of the subsequent cooling cycle (i.e., from 110 to 25 °C). Similarly, during the same variation of temperature, the hydraulic aperture of Specimen N19 decreased from 10.1 to 2.5 µm, and then further to 2.1 µm.

The fracture deformation observed during the experiments was caused by a combination of different effects, which in turn were distinctly affected by time, temperature, and pressure. Although these three modes of deformation are closely coupled in the experiments, some analyses can still be performed. Firstly, time-dependent deformation can be associated with the changes in hydraulic aperture observed during each step of experiments #N14-S1, #N14-S2, and #N14-S3 (Fig. 7a), as the temperature and pressure were constant at each step. After each temperature increase, the dilation of the specimen inherently needed a certain amount of time to be completed, as the thermal equilibrium was gradually reached and the matedness of the fracture surfaces progressively evolved.

Secondly, temperature-dependent deformation can be analyzed by comparing the final stages of two temperature steps, at the same confining pressure. Thirdly, pressure-dependent deformation can be inferred from the changes between the heating/cooling cycles of different groups of experiments, as the cycles differ in the confining pressure applied. Within the same experiment, however, not pressure-dependent, but rather temperature-dependent deformation is expected to be the main mode associated with the changes in hydraulic aperture, as the fracture surfaces have previously reached a steady state at each constant confining pressure when the heating/cooling cycles started. It is worth to note that, for each specimen, the experiments were conducted in sequence (#N14-S1→#N14-S2→#N14-S3 and #N19-C1→#N19-C2), thus, due to the complex, time-dependent nature of fracture surface accommodation, the possibility of cumulative effects of confining pressure increases in fracture closure should not be discarded for the second and third experiments of the sequences (experiments #N14-S2, #N14-S3 and #N19-C1). The three modes of deformation and their mechanisms will be further discussed in the following paragraphs.

With respect to temperature-dependent effects, an increase in temperature is expected to cause thermal expansion of the rock, resulting in a reduction of the fracture void space and eventually in a reduction of the fracture permeability. Furthermore, this expansion intensifies the stress magnitude at the contacting asperities, in cases where the rock is mechanically constrained (Jaeger et al. 2007). These additional thermal stresses can cause grinding of those asperities, which are in tight contact, creating gouge material and further reducing the overall hydraulic aperture. Even though the final temperature of 110 °C is in the range of moderated temperatures, heating has induced a decrease in the specimen's hydraulic apertures of 20–75% of their starting hydraulic aperture at 25 °C. Similar reductions in hydraulic apertures were reported by Faoro et al. (2016) for their flow-through experiments with artificially fractured granite, where a decrease of 37% in hydraulic aperture was observed due to an increase in temperature from 25 to 150 °C over a just 120 h. It has been reported that the effect of an increase in temperature on the hydraulic aperture varies according to several parameters, including rock type, specimen size, initial aperture field, and temperature variation (Faoro et al. 2016; Kamali-Asl et al. 2018). Although the involvement of multiple parameters in the dependence of hydraulic apertures on temperature variations complicates the comparison between different studies, the majority of the previously reported observations have shown reductions of 40–80% in hydraulic apertures of single fractures when submitted to a temperature increase to 90–150 °C from room temperature under a certain stress (Polak et al. 2003; Yasuhara et al. 2011; Faoro et al. 2016), congruent with the current experimental results.

The experimental results being consistent with previous studies are of great relevance, considering that the current tests were performed with natural granite fractures, not artificially induced fractures. These two types of fractures are supposed to respond differently to THMC effects. On the one hand, natural fractures are stiffer than induced fractures (Gale 1982), due to prior changes in surface roughness of the former, caused by weathering, dissolution, and precipitation (Cook 1992). Higher stiffness would lead to lower joint closure after increases in confining pressure, if the temperature is kept constant. On the other hand, if the temperature increases during the experiments, natural

fractures might undergo more pronounced closure than induced fractures, due to the conditions in which each type of fracture was formed. "Freshly made" laboratory fractures are extremely tight and rough, because they are usually made at laboratory temperature (Barton et al. 1985). In contrast, natural fractures were formed at elevated temperatures compared to ambient (Barton 2007). When natural fractures cool down, some mismatch in microscale across the joint walls is expected to occur, due to the different thermal expansion coefficients of their constitutive minerals. When submitted to high temperatures again, natural fractures should undergo heterogeneous thermal dilation that promotes overclosure (Barton 2007), due to better fit of the fracture surfaces. Therefore, predicting the difference in response of natural and induced fracture to increases in temperature is complex, as different aspects should be taken into account. Further studies are necessary to assess how each mechanism (i.e., thermal dilation, mechanical creep, and pressure dissolution) is individually influenced by the type of fracture. Thus far, the current results show that the responses of natural fractures to increases in temperature are similar to the ones previously reported on artificially induced fractures (Faoro et al. 2016; Yasuhara et al. 2011; Kamali-Asl et al. 2018).

Furthermore, hysteretic behavior is observed in the thermally driven changes in hydraulic apertures in both groups of experiments (Fig. 7a, b). The hydraulic apertures of Specimens N14 and N19 retain decreases of $\Delta b_{\text{hyd}} = 2.0$ μm and $\Delta b_{\text{hyd}} = 1.4$ μm, respectively, after heating up to 110 °C and cooling down back to 25 °C, under 20 MPa. Under 30 MPa, the hysteresis effect is even more pronounced, so that the residual decrements of $\Delta b_{\text{hyd}} = 5.4$ μm and $\Delta b_{\text{hyd}} = 8.0$ μm in hydraulic aperture width are observed for Specimens N14 and N19, respectively. Under the lower effective stress condition, the hysteresis effect is likely related to a tighter lock between the fracture surfaces, caused by the thermal dilation and mechanical creep, which is not fully recovered after the rock cools back down. This tighter lock can increase friction at the contacting asperities, preventing the reinstatement of the initial fracture spatial configuration (Barton 2007). The fact that the observed hysteresis effect was more pronounced for higher stresses suggests that additional mechanisms might have irreversibly shortened the fracture surface asperities, probably influenced by pressure-dependent mode of deformation. Pressure dissolution, plastic deformation, and gouge formation are examples of possible mechanisms that could happen in time periods as short as the ones applied in this study (Faoro et al. 2016). Previous studies have associated hysteresis effects with increased mating of opposing fracture surfaces and chemically mediated closure due to pressure dissolution (Barton 2007; Faoro et al. 2016; Kamali-Asl et al. 2018), which may also be the case in our current experiments.

For both the step-wise and the constant-rate heating experiments, the decrease in hydraulic aperture, triggered by thermal effects after the heating cycle (i.e., a full cycle), becomes more pronounced for larger normal stresses (i.e., 20 vs. 30 MPa), as shown in Fig. 7. Specifically, the full-cycle decreases in hydraulic apertures at 30 MPa normal stress are about 2 (Specimen N14) and 6 (Specimen N19) times larger than the decreases at 20 MPa normal stress. Higher normal stresses are expected to intensify the stress strength at the contacting asperities and/or to increase the contact area of the fracture surfaces (Pyrak-Nolte and Morris 2000; Yasuhara and Elsworth 2008), following pressure-dependent deformation, thereby enhancing thermal effects on fracture
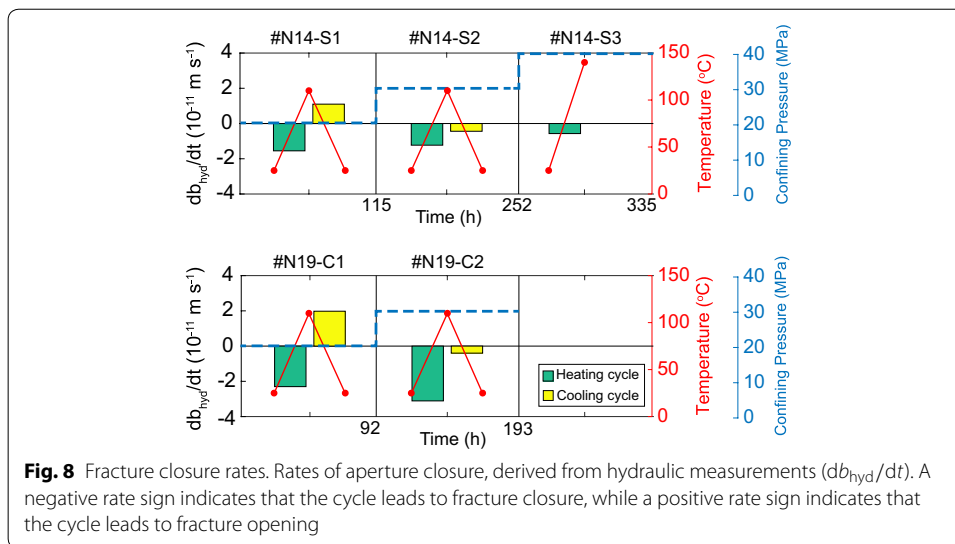
permeability. Even more pronounced fracture compaction has been observed by Kamali-Asl et al. (2018) when higher confining pressures were applied in their flow-through experiments. They associated this stronger compaction to more severe pressure dissolution, caused by an increase in the number of contacting asperities. However, we have not observed this trend in the present study when the confining stress was increased further to 40 MPa in the first group of experiments (Fig. 7a). In spite of the larger confining stress (i.e., 40 MPa), a less-pronounced fracture closure was observed, suggesting irreversible abrasion of contacting asperities and corresponding increases in matedness of the fracture surfaces. This increased matedness reduces the impact of further temperature increases, as the mated fractures undergo less joint closure due to increased confining stress (Jaeger et al. 2007).

The hydraulic aperture measurements yield the average rate of aperture closure, db_{hyd}/dt (m), for each cycle of increasing/decreasing temperature (Table 4 and Fig. 8). The magnitude of the calculated average aperture closure rate is between 10^{-11} to 10^{-12} m/s. A negative rate sign indicates that the cycle leads to fracture closure, which was the case for all heating cycles. In the cooling cycles under a confining pressure of 20 MPa, the aperture closure rates were positive, indicating a re-opening of the fracture, as the fracture aperture partially recovers from the thermal effects. However, in contrast to the expected re-opening trend, the aperture closure rates were negative under 30 MPa during the cooling cycles for both Specimens N14 and N19 (Fig. 8). The closure of fractures is shown as a lagging decrease of less than 1 μm in hydraulic apertures (Fig. 7). We hypothesize that this small decrease in hydraulic aperture, during cooling, might still have been caused by the previous heating cycle, from 25 to 110 °C (Table 4), because the thermal–mechanical effects, causing fracture compaction, are usually time-dependent (Yasuhara and Elsworth 2008). A similar trend was observed by Faoro et al. (2016) in flow-through experiments with single-fracture specimens, where the hydraulic aperture experienced a further decrease during the subsequent cooling cycle, after a previous heating cycle, under confining pressure of 40 MPa. Either the mechanical fracturing of asperities, such as subcritical cracking growth (Yasuhara et al. 2011), or mineral dissolution around contacting asperities, such as pressure dissolution, requires much longer time to reach an equilibrium state, particularly under higher confining stress. This time

Table 4 Fracture closure

Experiment	P_{co_r} (MPa)	T_i (°C)	T_f (°C)	Δt (h)	b_{hi} (μm)	b_{hf} (μm)	db_{hyd}/dt $(10^{-11}$ m/s)
#N14-S1	20	25	110	70	11.19	7.25	− 1.55
		110	25	44	7.25	9.00	+ 1.10
#N14-S2	30	25	110	85	8.32	4.56	− 1.23
		110	25	52	4.56	3.74	− 0.44
#N14-S3	40	25	140	83	3.30	1.61	− 0.57
#N19-C1	20	25	110	51	12.00	7.74	− 2.30
		110	25	41	7.74	10.65	+ 1.98
#N19-C2	30	25	110	67	10.06	2.54	− 3.11
		110	25	34	2.54	2.06	− 0.40

Hydraulic measurements of hydraulic aperture (b_{hyd}), where T_i and T_f are the temperatures at the beginning and at the end of the respective cycle, Δt is the duration of the cycle, b_{hi} and b_{hf} are the hydraulic apertures at the beginning and at the end of the respective cycle, and P_{co_r} is the radial confining pressure

Fig. 8 Fracture closure rates. Rates of aperture closure, derived from hydraulic measurements (db_{hyd}/dt). A negative rate sign indicates that the cycle leads to fracture closure, while a positive rate sign indicates that the cycle leads to fracture opening

lag might induce a counteraction to the cooling effect, such that a decrease in hydraulic aperture was observed during the cooling cycle in the laboratory experiments (Fig. 7).

Chemical measurements and analyses

As stated in the methodology section, the effluent fluid was collected in the receiving pump (Pump 3 in Fig. 4) at constant fluid pressure. After each complete cycle of increasing/decreasing temperatures, fluid in Pump 3 was sampled to determine the ion concentrations of the elements Al, Ca, Fe, K, Na, Mg, Ca, and Si [C_p (kg m^{-3})] (Table 5). As shown by Eq. 3, these measured ion concentrations are cycle-averaged concentrations for that specific cycle. For completeness, the total volume of fluid passed through the fracture in each cycle is listed in the last column of Table 5. Moreover, the mean release rate of each measured element was calculated for each cycle, by dividing the mean ion molar concentration by the cycle duration (Fig. 9). These element-wise mean release rates were compared to the mean release rate of silicon (Table 6). Compared to the influent, the increased concentrations of the measured elements are certainly associated with the dissolution of minerals, most probably due to mineral pressure dissolution (Kamali-Asl et al. 2018). Silicon was observed to be released at the highest rates during the experiments. This observation agrees with other studies that have reported that elevated temperatures enhance the dissolution rate of quartz (SiO_2) in water flow-through experiments (Savage et al. 1992; Yasuhara et al. 2011). In the first group of our experiments (Fig. 9a), the low ratios between the mean release rates of Si and Ca (Table 6) suggest that the dissolution of plagioclase (more specifically anorthite, based on our assumptions) was also significant in Specimen N14. In experiment #N14-S2, for example, the production of all elements, except Ca and Si, was negligible. The dissolution rate of anorthite ($CaAl_2Si_2O_8$) is on average 100 times higher than the dissolution rates of the other minerals (Yasuhara et al. 2011). Thus, the concentrations of Ca and Si were indeed expected to be the first ones to increase in the effluent, considering that the specimens have $\sim$30% of plagioclase (Table 3). During the heating cycle, under the highest confining pressure of 40 MPa (experiment #N14-S3), the mean release rate of

Table 5 Effluent fluid chemistry

Experiment	Test conditions				Incremental concentrations and effluent fluid volume							
	P_{co_r} (MPa)	T_i (°C)	T_f (°C)	Δt (h)	Al (ppm)	Ca (ppm)	Fe (ppm)	K (ppm)	Na (ppm)	Mg (ppm)	Si (ppm)	Volume (cm³)
#N14-S1	20	25	110	70	0.00	0.41	0.01	1.07	2.34	0.04	1.31	213
		110	25	44	0.00	0.16	0.01	–[a]	0.09	0.00	0.54	132
#N14-S2	30	25	110	85	–[b]	0.05	0.00	–[a]	–[b]	–[b]	0.32	255
		110	25	52	–[b]	0.13	–[b]	–[a]	–[b]	–[b]	0.28	156
#N14-S3	40	25	140	83	0.01	0.06	0.00	–[a]	–[b]	–[b]	3.14	249
#N19-C1	20	25	110	51	0.00	0.73	0.02	1.59	7.93	0.14	1.45	154
		110	25	41	0.00	0.25	0.05	0.73	0.89	0.05	0.88	122
#N19-C2	30	25	110	67	0.00	0.15	0.00	0.29	0.30	0.02	0.44	202
		110	25	34	0.01	0.15	0.04	0.69	0.47	0.03	1.33	101

[a] Below detection limit

[b] Undetectable increment

Fig. 9 Effluent chemical analysis. Element-wise mean release rate, including the ranges associated with equipment error: **a** first group of experiments: #N14-S1, #N14-S2, and #N14-S3; **b** second group of experiments: #N19-C1 and #N19-C2
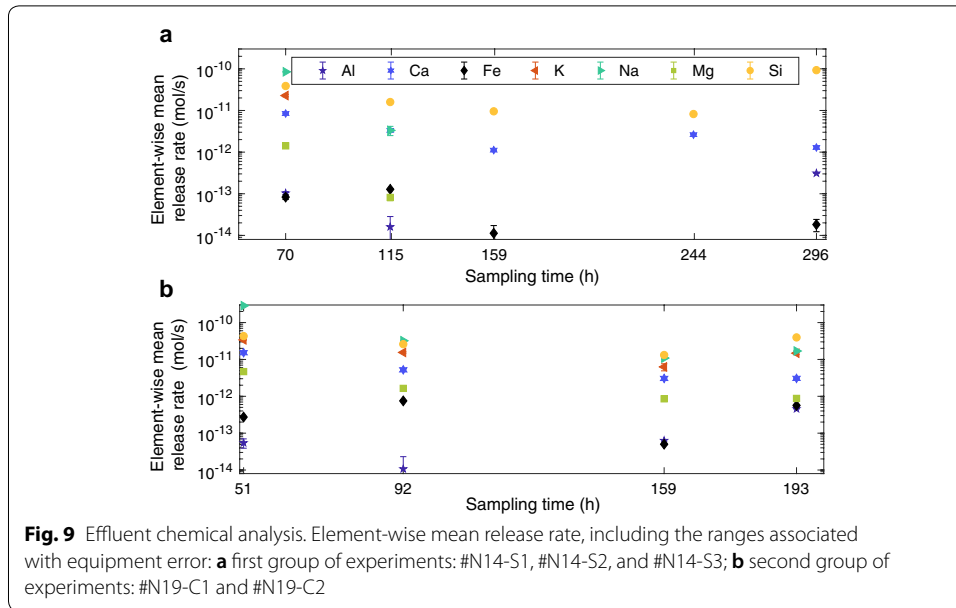
Table 6 Element-wise release rates

Experiment	Test conditions				Element-wise release rates						
	P_{co_r} (MPa)	T_i (°C)	T_f (°C)	Δt (h)	$\frac{Si}{Al}$	$\frac{Si}{Ca}$	$\frac{Si}{Fe}$	$\frac{Si}{K}$	$\frac{Si}{Na}$	$\frac{Si}{Mg}$	$\dot{M}_{Si}$ (10^{-11} mol s^{-1})
#N14-S1	20	25	110	70	>100	5	>100	2	0	27	3.876
		110	25	44	>100	5	>100	$-^a$	5	>100	1.596
#N14-S2	30	25	110	85	$-^b$	9	>100	$-^a$	$-^b$	$-^b$	0.955
		110	25	52	$-^b$	3	$-^b$	$-^a$	$-^b$	$-^b$	0.822
#N14-S3	40	25	140	83	>100	72	>100	$-^a$	$-^b$	$-^b$	9.304
#N19-C1	20	25	110	51	>100	3	>100	1	0	9	4.305
		110	25	41	>100	5	35	2	1	16	2.602
#N19-C2	30	25	110	67	>100	4	>100	2	1	15	1.318
		110	25	34	87	13	70	3	2	45	3.959

The ratios of the mean release rate of Si to the mean release rates of the other major elements, where $\dot{M}_t ext{Si}$ [mol s^{-1}] is the mean release rate of silicon

[a] Below detection limit

[b] Undetectable increment

silicon was 3 to 11 times higher than the silicon release rate in the other experiments with Specimen N14, which might have been due to the high dissolution rates of quartz under high temperatures (i.e., 140 °C) and large stresses. In the second group of experiments (Fig. 9b), the release rates of K and Na were as high as the rate of Si (Table 6), suggesting that dissolution of potassium feldspar and albite was significant in Specimen N19. In general, the concentrations of Al, Fe, and Mg in the effluent samples were less pronounced than the other elements, but the presence of Fe suggests that some biotite might have been dissolved.

Fig. 10 Fracture closure rates. Comparison between the rates of hydraulic aperture reduction, db_{hyd}/dt, and the chemical rates of aperture reduction, db_{chem}/dt, for four different estimated fractional contact areas: 1% (black diamond), 5% (black circle), 15% (black star), and 40% (square). **a** Step-wise heating experiments (#N14-S1, #N14-S2, and #N14-S3), with Specimen N14 under 3 different stresses (20, 30, and 40 MPa). **b** Constant-rate heating experiments (#N19-C1, #N19-C2), with Specimen N19 under 2 different stresses (20 and 30 MPa). Only the cycles that represent *closure* (i.e., originally negative rate) are compared

Estimation of contact area

To estimate the contact area for the pressure dissolution reactions during the thermally driven fracture closure, rates of aperture reduction, db_{chem}/dt [m], due to mineral dissolution, are determined from the effluent concentrations (Eq. 6), as explained in "Materials and methods" section. These chemical closure rates are then compared to the closure rates of hydraulic apertures, db_{hyd}/dt (m) (Table 4). The comparison is made for four hypothetical scenarios of fractional contact areas: 1, 5, 15, and 40% (Fig. 10). In Fig. 10, the absolute values of the rates are plotted, but only the results of the cycles that represent fracture *closure* (negative fracture closure rates, db_{hyd}/dt) are included for comparison (Table 4). The fractional contact area of a fracture can be estimated when $|db_{chem}/dt|$ is equivalent to $|db_{hyd}/dt|$, based on the assumption that time-dependent deformation is only controlled by pressure dissolution (Caulk et al. 2016). For Specimen N14, the fractional contact area of the fracture can be estimated as ~5% under confining pressures of 20 and 30 MPa, but under 40 MPa, the area increases to more than 40% (Fig. 10a). The increase of contact area agrees with the increased matedness of Specimen N14 during experiment #N14-S3, as previously discussed, because high fractional contact areas are expected for well-mated specimens (Caulk et al. 2016; Kamali-Asl et al. 2018). For Specimen N19, the estimated fractional contact area of the asperities ranges from 1% to 5% during the two heating cycles, but increases to around 40% during the cooling cycle under 30 MPa of confining pressure (Fig. 10b). The impact of chemical effects on fracture compaction was therefore higher during the cooling cycle under 30 MPa than during the previous cycles. Overall, considering the relatively short duration of the experiments (average of ~100 h as shown in Table 2) and the net effluent mass flux, the decrease in fracture permeability, observed in this study, may be associated with a *combined* effect of mechanical and pressure dissolution creep. The resultant responses from both mechanisms may be similar or indistinguishable.

Influence of fracture aperture distribution

Thermally driven fracture closure might also depend on the distribution of the fracture void spaces and their spatial correlation. Although the two specimens used in this study are both tensile fractures, their aperture fields exhibit some differences (Fig. 3). Compared to Specimen N14, the mean mechanical aperture of Specimen N19 is 2.2 times larger, the variance of the aperture distribution is 70% higher, and the spatial correlation length in the mean flow direction is 4.0 times larger (Table 1). Larger spatial correlation lengths tend to develop dominant preferential flow paths (Pyrak-Nolte and Morris 2000). In contrast, Specimen N14 is expected to present fewer regions of open fractures and more regions filled with numerous small, closely contacted regions (Pyrak-Nolte and Morris 2000). Therefore, an increase in thermal or normal stresses affects these two specimens differently. For the case of Specimen N19, the fracture is expected to be more compliant, due to the higher mean aperture (Jaeger et al. 2007). These features of Specimen N19 promote higher closure rates under the same increase of temperature or normal stress, as confirmed by experiments #N19-C1 and #N19-C2 (Specimen N19) during the heating cycles, where the hydraulic aperture variations were 1.1 and 2.0 times larger than those observed in Experiments #N14-S1 and #N14-S2 (Specimen N14) during the heating cycles (Fig. 7), respectively. Additionally, the total dissolved mineral mass from Specimen N19 was higher than the total dissolved mass from Specimen N14, when comparing similar cycles (Table 5). The relatively lower chemical dissolution rates, observed in Specimen N14, may be associated with a larger *initial* contact area (Fig. 10), as the contact area is more uniformly distributed in uncorrelated fractures (Pyrak-Nolte and Morris 2000). The larger contact area at the start of the experiments could ultimately have promoted less stress concentrations at the asperities during the experiments and therefore less pressure dissolution in Specimen N14.

Application to EGS

In order to guarantee the success and longevity of an EGS project, some production indicators are not intended to decrease over time, such as the flow rate, the production temperature, and the associated electricity generation (Caulk et al. 2016). However, if the permeability of the fracture network of an enhanced geothermal system decreases, these three indicators will naturally decrease. The fracture permeability may decrease due to different coupled THMC processes, as seen in the experimental results in this study, which can decline the production and impair the development of EGS at fully commercial scales (Kamali-Asl et al. 2018; Tester and DiPippo 2006). More specifically, in this study, the thermally driven fracture closure was modeled as a result of pressure dissolution, thermal dilation, and mechanical creep. The processes investigated in this study are expected to arise during operation of EGS, as cycles of multistage pressurized stimulation of the natural fractures (Ghassemi 2012) and formation of new fractures (Tomac and Gutierrez 2017) are expected as part of the establishment of the operational fracture network of the site. Once THMC processes lead to decrease in fracture aperture, this local permeability decrease can readily affect the entire fracture network, since it may reduce the connectedness of the network. While the results of the current study point out to the risk of injectivity impairment in a single fracture due to changes

in temperature and effective normal stress, further numerical studies considering field-scale fracture networks should be performed. These field-scale simulations enable feasibility predictions of EGS operations and thereby aid in accessing the EGS potential as an economically viable renewable energy production system.

Conclusions

The impact of temperature on hydraulic aperture widths and fracture permeabilities is investigated using a series of laboratory flow-through experiments on distinct naturally fractured GTS granite specimens at temperatures of 25–140 °C and effective normal stresses of 5–25 MPa.

Results show a decrease in the hydraulic aperture of natural fractures of 20–75% for moderate temperature increases, which is similar to the results observed in artificially induced fractures from previous studies. Short test durations (average of 100 h per loading/unloading cycle) and the chemical analysis of the effluent samples suggest that the decrease in hydraulic aperture is caused by thermal dilation, mechanical creep, and pressure dissolution, triggered by high temperatures. These effects are intensified by the magnitude of the normal confining stress applied to the fracture, as is evident from the 10–30% higher decreases in hydraulic aperture under 30 MPa normal stress, when compared to 20 MPa. Late effects of confining pressure increases, in sequential experiments, may also have contributed to the results observed, as fracture closure submitted to THMC effects is time-dependent. Additionally, under 30 MPa, the decreases in hydraulic aperture are noticeably irreversible, as the fracture permeability does not fully recover by the end of the loading cycles. This strong coupling between thermal effects and normal stresses is not unexpected, as mechanical creep and pressure dissolution act at contacting asperities of the fracture surfaces and are both intensified by compressive stresses at the contact points.

Analysis of the aperture distribution and spatial correlation of each specimen shows more pronounced thermal effects on fracture permeability for the specimen with larger mean mechanical aperture width and larger spatial correlation. Although temperature changes were conducted in steps in one group of experiments and at a constant rate in the other group of experiments, the results were comparable, suggesting that THMC effects can be observed over short timescales.

The laboratory results need to be upscaled to assess the impact of temperature variation on permeability of fracture networks at field scales. Nonetheless, this study highlights the importance of thermally driven fracture closure, as this can compromise the long-term operation of enhanced or engineered geothermal systems, or the operation of any reservoir, where the operation performance depends strongly on the transmissivity of natural or stimulated fractures.

Additional file

Additional file 1. The full details of the ICP-OES measurements of ion concentration, the operating condition of the ICP-OES instrument, the selected emission lines, the calibration range, the control sample, and the spike concentrations.

Author details
[1] Geothermal Energy and Geofluids Group, Institute of Geophysics, ETH Zürich, Sonneggstrasse 5, 8092 Zurich, Switzerland. [2] Laboratory of Inorganic Chemistry, D-CHAB, ETH Zürich, Vladimir Prelog Weg 1, 8093 Zurich, Switzerland. [3] Rock Deformation Laboratory, Institute of Geology, ETH Zürich, Sonneggstrasse 5, 8092 Zurich, Switzerland.

References
Amann F, Gischig V, Evans K, Doetsch J, Jalali R, Valley B, Krietsch H, Dutler N, Villiger L, Brixel B, Klepikova M, Kittilä A, Madonna C, Wiemer S, Saar MO, Loew S, Driesner T, Maurer H, Giardini D. The seismo-hydromechanical behavior during deep geothermal reservoir stimulations: open questions tackled in a decameter-scale in situ stimulation experiment. Solid Earth. 2018;9(1):115–37. https://doi.org/10.5194/se-9-115-2018.

Ameli P, Elkhoury JE, Morris JP, Detwiler RL. Fracture permeability alteration due to chemical and mechanical processes: a coupled high-resolution model. Rock Mech Rock Eng. 2014;47(5):1563–73.

Bandis SC, Lumsden AC, Barton NR. Fundamentals of rock joint deformation. Int J Rock Mech Min Sci Geomech Abstr. 1983;20(6):249–68. https://doi.org/10.1016/0148-9062(83)90595-8.

Barton N. Modelling rock joint behavior from in situ block tests: Implications for nuclear waste repository design. Office of Nuclear Waste Isolation, September: Technical report; 1982.

Barton N. Thermal over-closure of joints and rock masses and implications for HLW repositories. In: Proceedings of 11th ISRM Congress 2007;62:109–116.

Barton N, Bandis S, Bakhtar K. Strength, deformation and conductivity coupling of rock joints. Int J Rock Mech Min Sci Geomech Abstr. 1985;22:121–40.

Bažant ZP, Ohtsubo H. Stability conditions for propagation of a system of cracks in a brittle solid. Mech Res Commun. 1977;4(5):353–66. https://doi.org/10.1016/0093-6413(77)90015-5.

Blaisonneau A, Peter-Borie M, Gentier S. Evolution of fracture permeability with respect to fluid/rock interactions under thermohydromechanical conditions: development of experimental reactive percolation tests. Geotherm Energy. 2016;4(1):3. https://doi.org/10.1186/s40517-016-0045-9.

Brown SR, Kranz RL, Bonner BP. Correlation between the surfaces of natural rock joints. Geophys Res Lett. 1986. https://doi.org/10.1029/GL013i013p01430.

Brush DJ, Thomson NR. Fluid flow in synthetic rough-walled fractures: Navier–Stokes, Stokes, and local cubic law simulations. Water Resour Res. 2003;39:1. https://doi.org/10.1029/2002WR001346.

Caulk RA, Ghazanfaria E, Perdrialb JN, Perdrial N. Experimental investigation of fracture aperture and permeability change within enhanced geothermal. Geothermics. 2016;62:12–21. https://doi.org/10.1016/j.geothermics.2016.02.003.

Cook NGW. Natural joints in rock: mechanical, hydraulic and seismic behaviour and properties under normal stress. Int J Rock Mech Min Sci Geomech Abstr. 1992;29(3):198–223.

Dobrynin VM. Effect of overburden pressure on some properties of sandstones. Soc Pet Eng. 1962. https://doi.org/10.2118/461-PA.

Dobson PF, Kneafsey TJ, Sonnenthal EL, Spycher N, Apps JA. Experimental and numerical simulation of dissolution and precipitation: implications for fracture sealing at Yucca Mountain, Nevada. J Contam Hydrol. 2003;62–63:459–76. https://doi.org/10.1016/S0169-7722(02)00155-9.

Domenico PA, Schwartz FW. Physical and chemical hydrogeology. New York: J. Wilson & Sons; 1990.

Dusseault MB. Geomechanical challenges in petroleum reservoir exploitation. KSCE J Civil Eng. 2011;15(4):669–78.

Elliott D, Rutter E. The kinetics of rock deformation by pressure solution. Philos Trans R Soc A Math Phys Eng Sci. 1976;283:218–9. https://doi.org/10.1098/rsta.1976.0079.

Elsworth D, Yasuhara H. Mechanical and transport constitutive models for fractures subject to dissolution and precipitation. Int J Numer Anal Methods Geomech. 2010;34(5):533–49. https://doi.org/10.1002/nag.831.

Faoro I, Elsworth D, Candela T. Evolution of the transport properties of fractures subject to thermally and mechanically activated mineral alteration and redistribution. Geofluids. 2016;16:396–407. https://doi.org/10.1111/gfl.12157.

Gale JE. The effects of fracture type (induced versus natural) on the stress-fracture closure-fracture permeability relationships. In: Proceedings—the 23rd U.S symposium on rock mechanics (USRMS). American Rock Mechanics Association; 1982.

Gentier S, Riss J, Archambault G, Flamand R, Hopkins D. Influence of fracture geometry on shear behavior. Int J Rock Mech Min Sci. 2000;37(1):161–74. https://doi.org/10.1016/S1365-1609(99)00096-9.

Ghassemi A. A review of some rock mechanics issues in geothermal reservoir development. Geotech Geol Eng. 2012;30(3):647–64. https://doi.org/10.1007/s10706-012-9508-3.

Ghassemi A, Kumar GS. Changes in fracture aperture and fluid pressure due to thermal stress and silica dissolution/precipitation induced by heat extraction from subsurface rocks. Geothermics. 2007;36(2):115–40. https://doi.org/10.1016/j.geothermics.2006.10.001.

GOM: GOM: Atos core. http://www.atos-core.com/en/industries.php. Accessed 02 Feb 2019.

Hardin E, Barton N, Voegele M, Board M, Lingle R, Pratt H, Ubbes W. Measuring the thermomechanical and transport properties of a rockmass using the heated block test. In: Proceedings of the 23rd U.S Symposium on Rock Mechanics (USRMS), Berkeley, California 1982.

Huo D, Benson S. Experimental investigation of stress-dependency of relative permeability in rock fractures. Transp Porous Media. 2016;. https://doi.org/10.1007/s11242-016-0713-z.

Jacobs TDB, Junge T, Pastewka L. Quantitative characterization of surface topography using spectral analysis. Surf Topogr Metrol Prop. 2017;5(1):013001.

Jaeger JC, Cook NGW, Zimmerman R. Fundamentals of rock mechanics. Malden: Wiley-Blackwell; 2007. ISBN: 978-0-632-05759-7.

Kamali-Asl A, Ghazanfari E, Perdrial N, Bredice N. Experimental study of fracture response in granite specimens subjected to hydrothermal conditions relevant for enhanced geothermal systems. Geothermics. 2018;72:205–24. https://doi.org/10.1016/j.geothermics.2017.11.014.

Kim J, Sonnenthal E, Rutqvist J. A sequential implicit algorithm of chemo-thermo-poro-mechanics for fractured geothermal reservoirs. Comput Geosci. 2015;76:59–71. https://doi.org/10.1016/j.cageo.2014.11.009.

Kling T, Vogler D, Pastewka L, Amann F, Blum P. Numerical simulations and validation of contact mechanics in a granodiorite fracture. Rock Mech Rock Eng. 2018;51(9):2805–24.

Kopp A, Ebigbo A, Bielinski A, Class H, Helmig R. Numerical simulation of temperature changes caused by CO_2 injection in geological reservoirs. In: Grobe M, Pashin JC, Dodge RL, editors. Carbon dioxide sequestration in geological media— state of the science: AAPG studies in geology, vol. 59; 2009, pp. 439–456. https://doi.org/10.1306/13171 255St593391.

Kranzz RL, Frankel AD, Engelder T, Scholz CH. The permeability of whole and jointed barre granite. Int J Rock Mech Min Sci Geomech Abstr. 1979;16(4):225–34. https://doi.org/10.1016/0148-9062(79)91197-5.

Kumar GS, Ghassemi A. Numerical modeling of non-isothermal quartz dissolution/precipitation in a coupled fracture-matrix system. Geothermics. 2005;34(4):411–39. https://doi.org/10.1016/j.geothermics.2005.04.003.

Lang PS, Paluszny A, Zimmerman RW. Evolution of fracture normal stiffness due to pressure dissolution and precipitation. Int J Rock Mech Min Sci. 2016;88:12–22. https://doi.org/10.1016/j.ijrmms.2016.06.004.

Lee Y-K, Park J-W, Song J-J. Model for the shear behavior of rock joints under CNL and CNS conditions. Int J Rock Mech Min Sci. 2014;70:252–63. https://doi.org/10.1016/j.ijrmms.2014.05.005.

Liu HH, Ranjith PG, Georgi DT, Lai BT. Some key technical issues in modelling of gas transport process in shales: a review. Geomech Geophys Geo-Energy Geo-Resour. 2016;2(4):231–43.

Long JCS, Aydin A, Brown SR, Einstein HH, Hestir K, Hsieh PA, Myer LR, Nolte KG, Norton DL, Olsson OL, Paillet FL, Smith JL, Thomsen L. Rock fractures and fluid flow. Washington, D.C: National Academies Press, National Research Council; 1996.

Lowell R, Van Cappellen P, Germanovich LN. Silica precipitation in fractures and the evolution of permeability in hydrothermal upflow zones. Science. 1993;260:192–4. https://doi.org/10.1126/science.260.5105.192.

Luhmann AJ, Kong X-Z, Tutolo BM, Ding K, Saar MO, Seyfried WE Jr. Permeability reduction produced by grain reorganization and accumulation of exsolved CO_2 during geologic carbon sequestration: a new CO_2 trapping mechanism. Environ Sci Technol. 2012;47(1):242–51.

Luhmann AJ, Kong X-Z, Tutolo BM, Garapati N, Bagley BC, Saar MO, Seyfried WE Jr. Experimental dissolution of dolomite by CO_2-charged brine at 100 °C and 150 bar: evolution of porosity, permeability, and reactive surface area. Chem Geol. 2014;380:145–60.

Luo J, Zhu Y, Guo Q, Tan Y, Zhuang L, Liu M, Zhang C, Xiang W, Rohn J. Experimental investigation of the hydraulic and heat-transfer properties of artificially fractured granite. Nat Sci Rep. 2017. https://doi.org/10.1038/srep39882.

Luo J, Qi Y, Zhao Q, Tan L, Xiang W, Rohn J. Investigation of flow and heat transfer characteristics in fractured granite. Energies. 2018. https://doi.org/10.3390/en11051228.

Ma J, Querci L, Hattendorf B, Saar MO, Kong X.-Z. Towards a spatio-temporal understanding on dolomite dissolution in sandstone by CO_2-enriched brine circulation. Under review; 2019.

Martin JT, Lowell RP. Precipitation of quartz during high-temperature, fracture-controlled hydrothermal upflow at ocean ridges: equilibrium versus linear kinetics. J Geophys Res Solid Earth. 2000. https://doi.org/10.1029/1999JB900342.

Moore D, Lockner D, Byerlee JD. Reduction of permeability in granite at elevated temperatures. Science. 1994;265:1558–61. https://doi.org/10.1126/science.265.5178.1558.

Morrow CA, Moore DE, Lockner DA. Permeability reduction in granite under hydrothermal conditions. J Geophys Res. 2001;106:30551–60.

Lima *et al. Geotherm Energy*   (2019) 7:23

Page 27 of 28

Nguyen TS, Selvadurai APS. Coupled thermal-mechanical-hydrological behaviour of sparsely fractured rock: implications for nuclear fuel waste disposal. Int J Rock Mech Min Sci Geomech Abstr. 1995;32(5):465–79. https://doi.org/10.1016/0148-9062(95)00036-G.

Oron AP, Berkowitz B. Flow in rock fractures: the local cubic law assumption reexamined. Water Resour Res. 1998;34(11):2811–25.

Pandey SN, Vishal V. Sensitivity analysis of coupled processes and parameters on the performance of enhanced geothermal systems. Nat Sci Rep. 2017. https://doi.org/10.1038/s41598-017-14273-4.

Polak A, Elsworth D, Yasuhara H, Grader AS, Halleck PM. Permeability reduction of a natural fracture under net dissolution by hydrothermal fluids. Geophys Res Lett. 2003;. https://doi.org/10.1029/2003GL017575.

Pyrak-Nolte LJ, Morris JP. Single fractures under normal stress: the relation between fracture specific stiffness and fluid flow. Int J Rock Mech Min Sci. 2000;37:245–62.

Renshaw CE. On the relationship between mechanical and hydraulic apertures in rough-walled fractures. J Geophys Res Solid Earth. 1995;100:24629–36. https://doi.org/10.1029/95JB02159.

Ruistuen H, Teufel LW, Rhett D. Influence of reservoir stress path on deformation and permeability of weakly cemented sandstone reservoirs. SPE Reserv Eval Eng. 1999. https://doi.org/10.2118/56989-PA.

Rutqvist J, Tsang C-F. A study of caprock hydromechanical changes associated with CO_2 injection into a brine aquifer. Environ Geol. 2002;42:296–305. https://doi.org/10.1007/s00254-001-0499-2.

Rutqvist J, Freifeld B, Min K-B, Elsworth D, Tsang Y. Analysis of thermally induced changes in fractured rock permeability during 8 years of heating and cooling at the Yucca Mountain Drift Scale test. Int J Rock Mech Min Sci. 2008;45(8):1373–89. https://doi.org/10.1016/j.ijrmms.2008.01.016.

Savage D, Bateman K, Richards HG. Granite–water interactions in a flow-through experimental system with applications to the Hot Dry Rock geothermal system at Rosemanowes, Cornwall, UK. Appl Geochem. 1992;7(3):223–41. https://doi.org/10.1016/0883-2927(92)90039-6.

Schaltegger U. Geochemische und isotopengeochemische Untersuchungen am Zentralen Aaregranit und seinen assoziierten Gesteinen zwischen Aare und Reuss (Aarmassiv, Schweiz). Ph.D. thesis, University of Bern; 1989.

SciFinder: database of chemicals. https://scifinder.cas.org/scifinder. Accessed 13 Apr 2019.

Stalder HA. Petrographische und mineralogische Untersuchungen im Grimselgebiet (Mittleres Aarmassiv). Schweiz Mineral Petrogr Mitt. 1964;44:187–398.

Stephansson O, Jing L, Tsang CF. Coupled thermo-hydro-mechanical processes of fractured media. Amsterdam: Elsevier Science; 1996.

Tanaka Y, Miyakawa K, Fukahori D, Kiho K, Goto K. Survey of flow channels in rock mass fractures by resin injection. In: ISRM international symposium—8th Asian rock mechanics symposium, 14–16 October, Sapporo, Japan; 2014.

Taron J, Elsworth D. Coupled mechanical and chemical processes in engineered geothermal reservoirs with dynamic permeability. Int J Rock Mech Min Sci. 2010;47(8):1339–48. https://doi.org/10.1016/j.ijrmms.2010.08.021.

Tester J, DiPippo R. The future of geothermal energy: impact of enhanced geothermal systems (EGS) on the United States in the 21st Century. Massachusetts Institute of Technology: Technical report; 2006.

Toeroek A, Toeroek A. The effect of temperature on the strength of two different granites. Central Eur Geol. 2015;58(4):356–3697. https://doi.org/10.1556/24.58.2015.4.5.

Tomac I, Gutierrez M. Coupled hydro-thermo-mechanical modeling of hydraulic fracturing in quasi-brittle rocks using BPM-DEM. J Rock Mech Geotech Eng. 2017;9(1):92–104. https://doi.org/10.1016/j.jrmge.2016.10.001.

Tsang CF. Coupled processes associated with nuclear waste repositories. Orlando: Academic Press; 1987. ISBN 978-0-12-701620-7.

Tutolo BM, Luhmann AJ, Kong X-Z, Saar MO, Seyfried WE Jr. Experimental observation of permeability changes in dolomite at CO_2 sequestration conditions. Environ Sci Technol. 2014;48(4):2445–52.

Tutolo BM, Luhmann AJ, Kong X-Z, Saar MO, Seyfried WE Jr. CO_2 sequestration in feldspar-rich sandstone: coupled evolution of fluid chemistry, mineral reaction rates, and hydrogeochemical properties. Geochim Cosmochim Acta. 2015a;160:132–54.

Tutolo BM, Kong X-Z, Seyfried WE Jr, Saar MO. High performance reactive transport simulations examining the effects of thermal, hydraulic, and chemical (THC) gradients on fluid injectivity at carbonate CCUS reservoir scales. Int J Greenh Gas Control. 2015b;39:285–301.

Vogler D. Hydro-mechanically coupled processes in heterogeneous fractures: experiments and numerical simulations. Ph.D. thesis, ETH Zurich; 2016.

Vogler D, Amann F, Bayer P, Elsworth D. Permeability evolution in natural fractures subject to cyclic loading and gouge formation. Rock Mech Rock Eng. 2016;49(9):3463–79. https://doi.org/10.1007/s00603-016-1022-0.

Vogler D, Walsh SDC, Bayer P, Amann F. Comparison of surface properties in natural and artificially generated fractures in a crystalline rock. Rock Mech Rock Eng. 2017a;50(11):2891–909.

Vogler D, Walsh SDC, Dombrovski E, Perras MA. A comparison of tensile failure in 3D-printed and natural sandstone. Eng Geol. 2017b;226:221–35.

Vogler D, Settgast RR, Annavarapu C, Madonna C, Bayer P, Amann F. Experiments and simulations of fully hydro-mechanically coupled response of rough fractures exposed to high-pressure fluid injection. J Geophys Res Solid Earth. 2018;123:1186–200. https://doi.org/10.1002/2017JB015057.

Witherspoon PA, Wang JS, Iwai K, Gale JE. Validity of cubic law for fluid flow in a deformable rock fracture. Water Resour Res. 1980;16(6):1016–24.

Yasuhara H, Elsworth D, Polak A. Evolution of permeability in a natural fracture: significant role of pressure solution. J Geophys Res Solid Earth. 2004. https://doi.org/10.1029/2003JB002663.

Yasuhara H, Polak A, Mitani Y, Grader A, Halleck P, Elsworth D. Evolution of fracture permeability through reactive flow at elevated temperatures. Trans Geotherm Resour Council. 2005;29:437–41.

Yasuhara H, Polak A, Mitani Y, Grader AS, Halleck PM, Elsworth D. Evolution of fracture permeability through fluid-rock reaction under hydrothermal conditions. Earth Planet Sci Lett. 2006;244(1):186–200. https://doi.org/10.1016/j.epsl.2006.01.046.

Lima *et al. Geotherm Energy*   (2019) 7:23

Page 28 of 28

Yasuhara H, Elsworth D. Compaction of a rock fracture moderated by competing roles of stress corrosion and pressure solution. Pure Appl Geophys. 2008;165(7):1289–306.

Yasuhara H, Kinoshita N, Ohfuji H, Lee DS, Nakashima S, Kishida K. Temporal alteration of fracture permeability in granite under hydrothermal conditions and its interpretation by coupled chemo-mechanical model. Appl Geochem. 2011;26(12):2074–88. https://doi.org/10.1016/j.apgeochem.2011.07.005.

Yin T-B, Shu R-H, LI X-B, Wang P, Liu X-L. Comparison of mechanical properties in high temperature and thermal treatment granite. Trans Nonferr Metals Soc China. 2016;26(7):1926–37. https://doi.org/10.1016/S1003-6326(16)64311-X.

Yow JL, Wilder DG. Rock mass response to thermal loading and unloading at the spent fuel test. Rock Test Site Charact. 1993. https://doi.org/10.1016/B978-0-08-042066-0.50042-2.

Zhang R, Winterfeld PH, Yin X, Xiong Y, Wu Y-S. Sequentially coupled THMC model for CO_2 geological sequestration into a 2D heterogeneous saline aquifer. J Nat Gas Sci Eng. 2015;27:579–615. https://doi.org/10.1016/j.jngse.2015.09.013.

Zhang R, Xiong Y, Winterfeld P, Yin X, Wu Y-S. A novel computational framework for thermal-hydrological-mechanical-chemical processes of CO_2 geological sequestration into a layered saline aquifer and a naturally fractured enhanced geothermal system. Greenh Gases Sci Technol. 2016;6:370–400. https://doi.org/10.1002/ghg.1571.

Zimmerman RW, Kumar S, Bodvarsson GS. Lubrication theory analysis of the permeability of rough-walled fractures. Int J Rock Mech Min Sci Geomech Abstr. 1991;28(4):325–31. https://doi.org/10.1016/0148-9062(91)90597-F.

Publisher's Note

Springer Nature remains neutral with regard to jurisdictional claims in published maps and institutional affiliations.